Pure Appl. Geophys.

https://doi.org/10.1007/s00024-018-1983-x

Pure and Applied Geophysics

Near-Field Spectra of Large Earthquakes

Raul Madariaga,[1] Sergio Ruiz,[2] Efrain Rivera,[2,3] Felipe Leyton,[4] and Juan Carlos Baez[4]

Abstract—We have studied the spectra of large subduction earthquakes in Chile at short epicentral distances. In this work, we concentrate on the M_w 8.2, Iquique earthquake of 1 April 2014. For such a large event, in most stations we cannot separate P and S waves; which arrive very close together and interfere to produce the static displacement field. We find that the displacement spectra observed in all the accelerograms are significantly different from the usual far-field Brune spectrum. Displacement spectra have clear omega-1 decay at low frequencies that we prove to be associated with the dominant role of near and intermediate field waves in the ground motion. The origin of the omega-1 decay is that at short distances, displacement contains a finite static displacement. We confirm this spectral behavior by comparing the spectra computed from accelerograms integrated to velocity with co-located GNSS recordings. Both spectra are flat at low frequencies and the low-frequency asymptote of the velocity spectrum is proportional to the static displacement determined from GNSS. We explore the transition from these near-field records to far-field ones and find that the usual omega-2 spectrum appears only at large distances compared to the size of the dynamic rupture zone. For large earthquakes, the displacement spectra have a term proportional to the moment spectrum and another proportional to moment rate spectrum. The term proportional to moment dominates the low-frequency behavior of accelerograms in the near and intermediate field, so that they do not follow the omega-square decay of the moment rate spectrum.

Key words: Earthquakes, Chile, seismic spectra.

1. Introduction

Large earthquakes in subduction zones are particularly dangerous because they produce extensive damage, but their spectral characteristics in the near field have been only recently studied because of lack of local unclipped data. In Chile, we can use a combination of new geodetic and acceleration data to study the waves radiated by large earthquakes at low frequencies in addition to the best known high frequencies.

Northern Chile is an active seismic zone, where large-magnitude earthquake occur frequently (Ruiz and Madariaga 2018). The intraplate intermediate-depth event of 2005 Tarapacá M_w 7.8 (Delouis and Legrand 2007; Peyrat et al. 2006) prompted the deployment of seismological stations within the Integrated Plate Boundary Observatory Chile—IPOC, a multi-component network created by German, French and Chilean researchers (IPOC 2006). Since then, northern Chile earthquakes have been well recorded by GNSS, broadband and strong motion stations located on hard rock sites (Leyton et al. 2018a, b; Báez et al. 2018). The first large earthquake after the installation of IPOC was the M_w 7.7 Tocopilla earthquake of 2007 (Delouis et al. 2009; Peyrat et al. 2010; Schurr et al. 2012; Fuenzalida et al. 2013). Lancieri et al. (2012) studied the spectral characteristics of this earthquake and its aftershocks. They found that all aftershocks had a typical omega-squared spectrum (Aki 1967; Brune 1970; Madariaga 1976; Madariaga and Ruiz 2016). The main shock, on the other hand, had a different kind of spectrum that diverged at low frequencies, increasing like omega-1. At that time few accelerometers were available and these authors proposed that this behavior was probably due to near-field waves, but that it could also be due to the complexity of this double event. These observations suggested that the ground motion spectrum of large Chilean earthquakes was different in the near and intermediate field from the usual omega-squared

[1] Laboratoire de Géologie, PSL Université, Ecole Normale Supérieure and CNRS, 24 rue Lhomond, 75230 Paris Cedex 05, France. E-mail: madariag@geologie.ens.fr
[2] Department of Geophysics, Universidad de Chile, Blanco Encalada 2002, Santiago, Chile.
[3] Department of Geology, Universidad de Chile, Plaza Ercilla, Santiago, Chile.
[4] Centro Sismológico Nacional, Universidad de Chile, Blanco Encalada 2002, Santiago, Chile.

Published online: 13 September 2018

model proposed by Aki (1967) and Brune (1970) for events recorded in the far field.

The Aki–Brune spectrum has been successfully used to invert the dynamic characteristics of earthquake ruptures using far-field P or S waves (Abercrombie 1995; Ide and Beroza 2001; Prieto et al. 2004; Allmann and Shearer 2009; Oth et al. 2010; Lancieri et al. 2012; Archuleta and Ji 2016; Denolle and Shearer 2016; and many others). Here, we focus on a different aspect of spectral records, characterizing the behavior of large-magnitude earthquakes recorded with both GNSS and strong motion instruments in the near field.

The first very large Chilean earthquake recorded by modern seismological data was the 2010 M_w 8.8, Maule megathrust earthquake, which produced excellent continuous GNSS records that were used by Vigny et al. (2011) as seismograms to model this event. The displacement records of this earthquake had large static co-seismic displacements. Unfortunately, no digital good-quality accelerometers were located close to the epicenter of the Maule 2010 earthquake (Ruiz et al. 2012). After this earthquake, the Centro Sismologico National (CSN) of the University of Chile was created and deployed a large network of broadband, accelerometers and GNSS stations (Barrientos et al. 2018; Leyton et al. 2018a, b; Báez et al. 2018). These stations that include now those installed by IPOC have recorded several large earthquakes, such as the M_w 8.2 Iquique event of 1 April 2014, the M_w 8.3 Illapel earthquake of 15 September 2015 and the M_w 7.6 Chiloé earthquake of 25 December 2016. These events provide excellent recordings that have been largely used to model the events and to study their principal characteristics (e.g., Ruiz et al. 2014, 2016, 2017a, b; Schurr et al. 2014; Hayes et al. 2014; Lay et al. 2014; Melgar et al. 2016, 2017; Tilmann et al. 2016; Ye et al. 2016; Lange et al. 2017). These studies have been centered on the slip distribution, tsunami effects, nucleation process and their relation with slow slip events, but overlook the spectral properties of strong motion records in the near field. Here, we examine the general properties of these accelerograms. We use the records written by the Iquique earthquake of 1 April 2014, because this is the Chilean earthquake with the largest number of co-located GNNS and strong motion records on hard rock sites (Leyton et al. 2018a; Báez et al. 2018). Our goal is to understand the basic features of displacement spectra, the relative role of low and high frequencies of the spectrum and their relation with the seismic moment and seismic moment rate histories.

2. *The Iquique Earthquake and Its Near Field*

On 1 April 2014, a magnitude M_w 8.2 hit the northern Chile region of Tarapacá near the City of Iquique, and 2 days later the largest aftershock with magnitude M_w 7.7 occurred (see Fig. 1) (Ruiz et al. 2014; Schurr et al. 2014; Hayes et al. 2014; Lay et al. 2014; Duputel et al. 2015). This event has been studied carefully because it was preceded by a long series of precursory shocks that began several years before 2014 and culminated in an intense, but intermittent series of foreshocks that started in July 2013 (León-Ríos et al. 2016; Cesca et al. 2016). A slow slip event was observed before the main shock that has been carefully documented (Ruiz et al. 2014; Kato and Nakagawa 2014; Socquet et al. 2017). The main event was studied by a number of researchers using a combination of far- and near-field data that were reviewed by Duputel et al. (2015) and, recently, its post-seismic deformation has been analyzed by Hoffmann et al. (2018).

The Iquique seismic sequence was recorded by a large set of multi-parameter stations of the IPOC networks. In addition to these data, several other acceleration and GNSS stations deployed by the CSN (Leyton et al. 2018a; Báez et al. 2018) are available. The full set of stations considered in this work are listed in Table 1 and plotted in Fig. 1.

The Iquique main shock started with an immediate foreshock located some 30 km ocean-ward of the main rupture. In Fig. 2, we plot the EW accelerograms at two stations, PSGCX and TA01, and their locations can be found in Fig. 1. The two records show that the Iquique event started with an immediate foreshock that occurred at 23:46:46 (T_1) and was followed by the main event at time T_2 = 23:47:03 (Ruiz et al. 2014). The difference between T_1 and T_2 (17 s) is larger than the arrival time of the S waves from the first event at many stations, so that after a

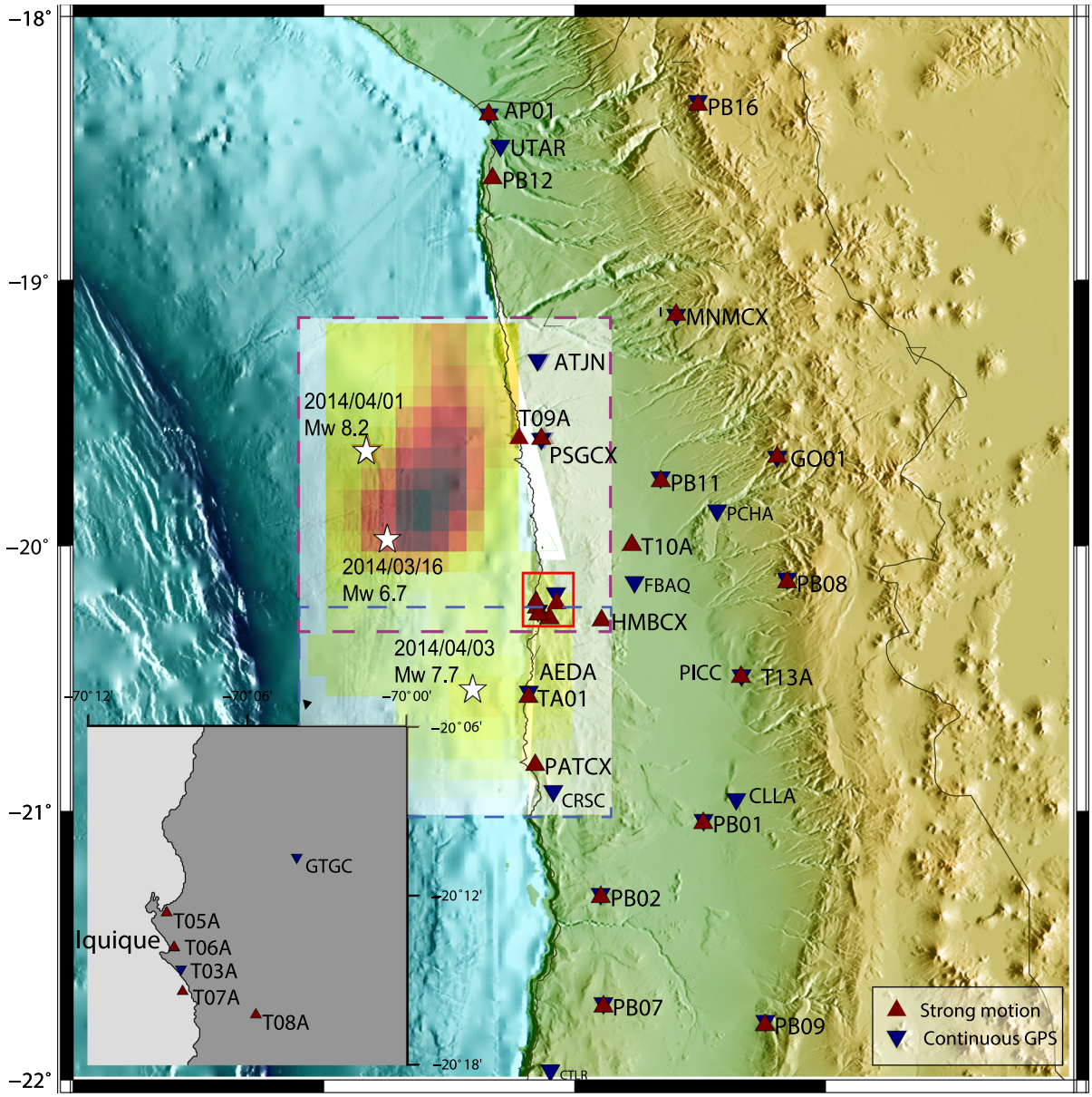

Figure 1
Map of northern Chile near the Iquique earthquake of 1 April 2014. The slip distribution of the main event and its main aftershock of 3 April 2014 are shown with colors (from Ruiz et al. 2014). White stars show the epicenters of both events in addition to the 16 March 2014 foreshock. The events are situated between the trench and the Chilean coastline along the plate interface. The main stations used in the present study are shown on the continent. The inset shows the instruments available around the City of Iquique

few seconds the P and S waves were mixed in the accelerograms. This prevents us from separating the P and S far-field waves associated with the rupture of the main slip patch (main asperity) of this large-magnitude event.

First, we focus on the recordings of the accelerometer at station PSGCX and the collocated PSGA GNSS site, both situated near the City of Pisagua in northern Chile. These stations are the closest to the epicenter of the nucleation foreshock as

Table 1

Northern Chile instruments

Code	Longitude	Latitude	Type
aeda	− 70.1777	− 20.54614	GNSS
atjn	− 70.136738	− 19.3008 0	GNSS
cbaa	− 68.448198	− 22.746394	GNSS
cdlc	− 69.761555	− 22.189982	GNSS
cgtc	− 70.068623	− 20.177139	GNSS
chm2	− 69.194134	− 19.668575	GNSS
clla	− 69.35664	− 20.95448	GNSS
chyt	− 70.342112	− 18.3708285	GNSS
cgtc	− 70.068623	− 20.177139	GNSS
chm2	− 69.194134	− 19.668575	GNSS
clla	− 69.35664	− 20.95448	GNSS
colc	− 68.638617	− 19.27621	GNSS
crsc	− 70.07976	− 20.91768	GNSS
ctlr	− 70.096824	− 21.964205	GNSS
fbaq	− 69.755396	− 20.134643	GNSS
mnmi	− 69.595661	− 19.131416	GNSS
pccl	− 70.106751	− 18.45766	GNSS
ptre	− 69.57451	− 18.19452	GNSS
pccl	− 70.106751	− 18.45766	GNSS
pcha	− 69.431944	− 19.869444	GNSS
picc	− 69.334617	− 20.489858	GNSS
psga	− 70.12301	− 19.59738	GNSS
ptre	− 69.57451	− 18.19452	GNSS
uapf	− 70.141388	− 20.243055	GNSS
utar	− 70.296388	− 18.490556	GNSS
GO01	− 69.1942	− 19.6686	ACCEL
MNMCX	− 69.5955	− 19.1311	ACCEL
PSGCX	− 70.1230	− 19.5972	ACCEL
HMBCX	− 69.8879	− 20.2782	ACCEL
PATCX	− 70.1529	− 20.8207	ACCEL
PB01	− 69.4874	− 21.0432	ACCEL + GNSS
PB02	− 69.8960	− 21.3197	ACCEL + GNSS
PB03	− 69.7531	− 22.0485	ACCEL + GNSS
PB07	− 69.8862	− 21.7267	ACCEL + GNSS
PB08	− 69.1534	− 20.1411	ACCEL + GNSS
PB09	− 69.2419	− 21.7964	ACCEL + GNSS
PB11	− 69.6558	− 19.7610	ACCEL + GNSS
PB12	− 70.3281	− 18.6141	ACCEL + GNSS

shown in Fig. 1. Figure 3 shows the displacement record obtained at the EW component of the GNSS geodetic station on top of which we have superposed the displacement field doubly integrated from the EW accelerogram recorded at the PSGCX accelerometer. The accelerogram was integrated using the method proposed by Boore (2001) which consists of isolating a central time window in the signal where the strongest motion is concentrated, and then removing the trend outside the window. Variations of this

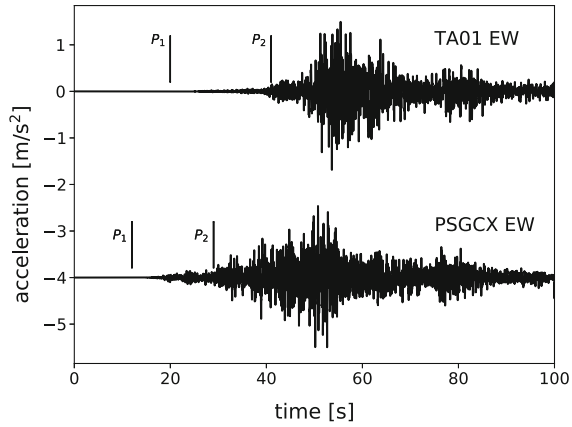

Figure 2

The 2014 Iquique main shock recorded at two near-field accelerograms located in Pisagua (PSGCX) and the Iquique airport (TA01). The zero line of the PSGCX record has been displaced by 4 s. The P1 and P2 arrows denote the times of first P-wave arrival from the immediate foreshock and the P-wave arrival from the main rupture, respectively. At these stations the P2 wave arrived at about the same time as the S wave generated by the immediate foreshock (P1)

technique have been proposed some time earlier and later extended by other authors (Graizer 1979, 2010; Iwan et al. 1985; Boore 2001; Wang et al. 2003, 2011, 2013; Boore and Bommer 2005; Wu and Wu 2007; Chao et al. 2009). In Fig. 3, we show with vertical lines the window that we isolated for the estimation of displacement using the procedure defined by Boore (2001). We verified that using different windows for the strong motion double integration procedure, we could fit the low-frequency features of the GNSS records. Additional examples of the fit between GNSS recordings and integrated accelerograms in Chile have been recently published by Báez et al. (2018).

3. *Computing Ground Motion Spectra from Accelerograms*

We will now compute the spectra of the records shown in Fig. 3. For large earthquakes in the near field, it is not possible to separate P and S waves because these waves are delayed by less time than the total seismic source duration of the earthquake. For the Iquique earthquake, the total duration is about 50 s (Figs. 2, 3). Figure 3 shows that the near-field

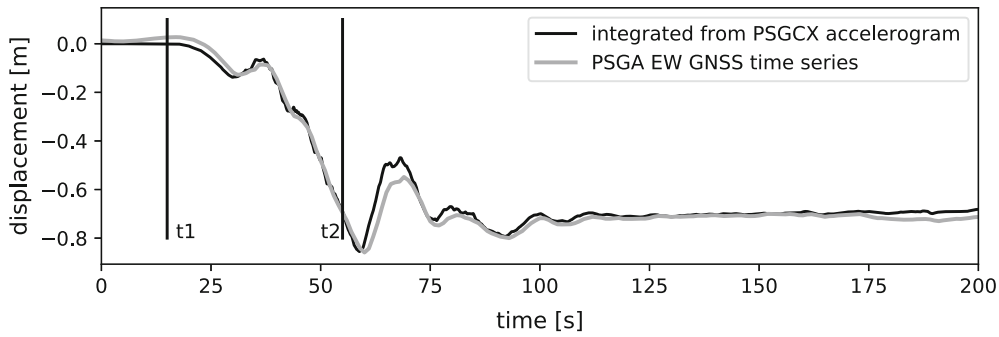

Figure 3
Comparison of the GNSS EW displacement at station PSGA (Pisagua) and that obtained from the integration of the collocated PSGCX accelerogram using Boore's (2001) method. The vertical lines define the beginning t_1 and end t_2 of the strong motion window used to integrate the accelerograms. The GNNS data has been corrected for leap seconds

term starts immediately after the arrival of P waves and decreases significantly before the S-wave arrival. After the end of the S waves (and possibly of surface waves), displacement becomes constant and approximately equal to the static displacement observed in the GNSS station PSGA.

Unfortunately, accelerograms processed by the Boore (2001) procedure cannot be used to compute spectra, because the removal of the base line is nonlinear. The spectra of the displacement signals computed in this way will contain the effect of the linear trends and the transition of the zero line in the strong-motion window. It is possible to improve the integration of accelerograms using displacement records obtained at collocated GPS instruments as proposed by several authors (e.g., Bock et al. 2011; Wang et al. 2013, among others). Unfortunately, even if the integration of accelerograms is improved, the displacement records still cannot be used to compute displacement spectra because of the finite displacement jump at the end of the record. The reason is that the numerical Fourier transform used to compute the spectra from signals like those of Fig. 3 assumes that the time series is periodic with a period equal to the duration of the record. Thus, the computed Fourier transform sees a jump in displacement at the end of the record and is contaminated at all frequencies. The Fourier transform of such a jump is simply $u_s/i\omega$, where u_s is the static displacement. All the other spectral information contained in the accelerogram is hidden by this jump. Many techniques have been proposed in the literature to remove this effect of the finite time window. Some of them consist in using a window to multiply the time signal, but these windows contaminate the low-frequency contents. In Fig. 4, we show the displacement spectrum computed directly from the displacement signal integrated by the Boore (2001) procedure shown in Fig. 3. In this figure, the numerical Fourier transform of the displacement trace is shown in black. As expected, it is a straight line of slope -1 with amplitude proportional to the static displacement. For this reason we have chosen a method that exploits the finiteness of the velocity time series. In the same figure, we plot in gray the displacement spectrum computed from the velocity traces using the method described in the next section

We propose a simple method to compute the displacement spectrum that uses a property of the velocity time series. The accelerograms integrated once to determine the ground velocity have been shown to be very well fitted at low frequencies by the ground velocity derived from GNSS signals (e.g., Báez et al. 2018). Figure 5 shows the three components of the ground velocity integrated from accelerograms at the PSGCX station, and the velocities derived from the PSGA GNSS recordings. The instrument response of the accelerograms was removed, and the records have been low-pass filtered with a causal Butterworth filter of order 2 and corner frequency 0.5 Hz. The coincidence between the records is excellent. This representation is better than comparisons between displacement records to show that the frequency content of the two records is the

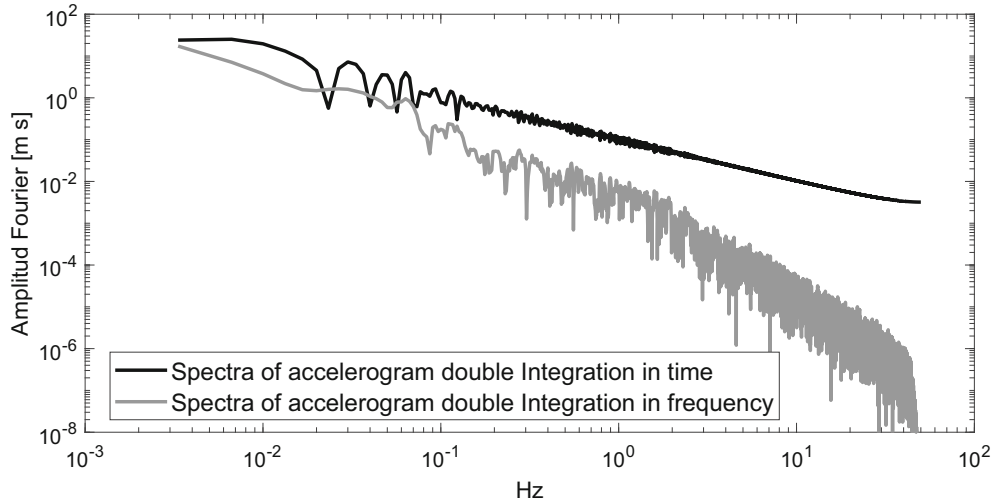

Figure 4
Finite Fourier transform of the displacement trace at station PSGCX shown in Fig. 3. The black spectrum was computed directly from displacement obtained by doubly integrating the accelerogram shown in Fig. 3, without correction for the jump in displacement at the end of the time series. In gray, we show the spectrum computed for the displacement obtained by double integration in the spectral domain (i.e., dividing the acceleration spectrum by ω^{-2})

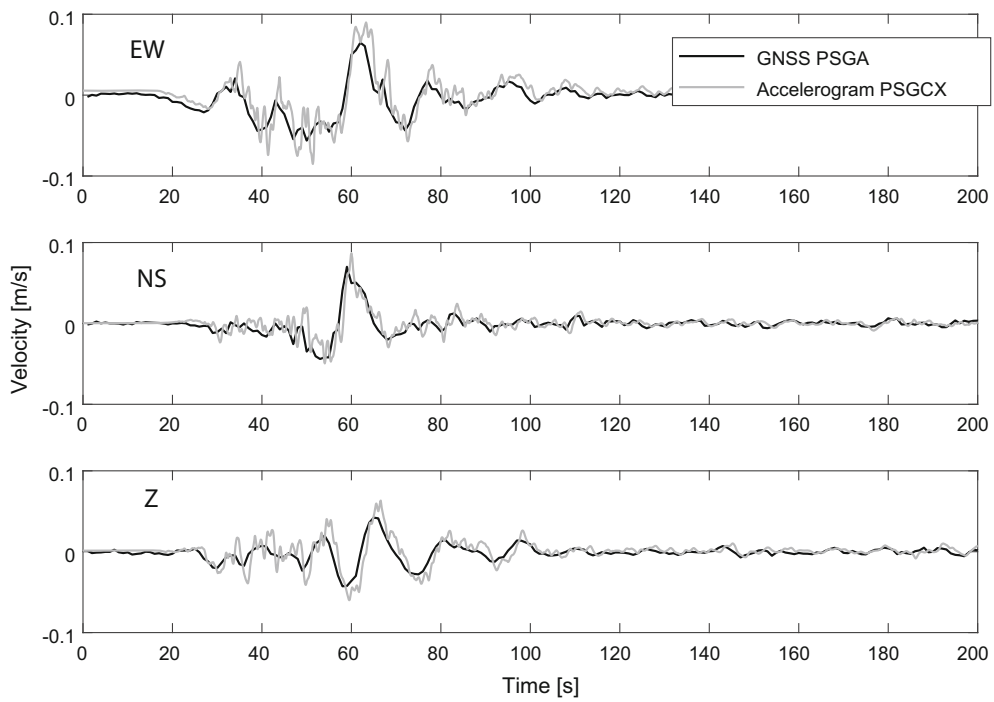

Figure 5
Comparison of ground velocity determined at the Pisagua stations from GNSS records (PSGA) and co-located integrated accelerogram (PSGCX). The velocity records obtained from accelerograms have been low-pass filtered at 0.5 Hz to enhance the similarity between these records in their common band pass

same in the frequency range where they both coincide (conservatively estimated as above 0.15 Hz).

In Fig. 6, we show the Fourier spectra of the velocity traces at station PSGCX plotted in Fig. 5. Since velocity returns to zero at the end of traces, except for seismic noise, we can compute the velocity spectrum without the problems of the finite displacement at the end of the time window discussed above for Figs. 3 and 4. The spectra computed using regular FFT routines display a common property of ground velocity for the Iquique and other large subduction earthquakes in Chile. The spectral trend is flat at low frequencies in contrast to predictions of far-field velocity radiation for finite sources (Brune 1970; Madariaga 1976) that should linearly increase with ω at low frequencies. A more detailed explanation will be provided in the next section, but it is relatively easy to understand. At close distances from the source, the near-field terms of the Green function dominate the radiated spectrum. The near field is dominated by the moment time function, not the moment rate, so that at close distances the velocity spectrum at low frequencies resembles that of the integral of the far-field source time function. We can now compute displacement spectra from the velocity spectra by simply dividing them by $i\omega$, that is, by the infinite integration operator in the frequency domain. The spectra thus calculated remove the spurious high-frequency ω^{-1} spectral decay of the Fourier transforms computed from a finite displacement time series in the near field. The displacement spectrum of the ground motion is shown in gray in Fig. 4.

A particular property of the velocity spectra in Fig. 6 is that the Fourier transform of the ground velocity in the near field must approach at low frequencies the static displacements observed in Fig. 3. From classical Fourier transform theory, the spectrum of ground velocity near zero frequency approaches

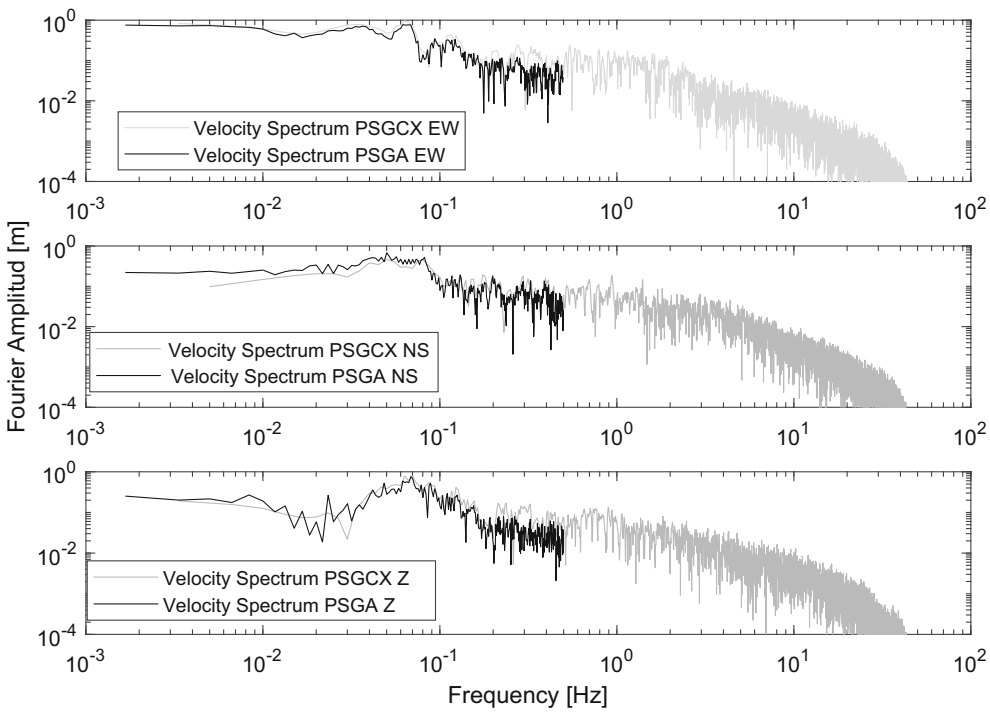

Figure 6
Spectra of the velocity records from the PSGA GNSS station and the PSGCX accelerogram. The time domain velocity signals are shown in Fig. 5. These spectra were directly computed using a fast Fourier transform algorithm. We observe that at low frequencies, the accelerogram and GNSS instrument share an almost identical spectrum in spite of the different noise levels in these two types of instrument. All three components have almost flat spectra at low frequencies. These low-frequency velocity spectra converge to co-seismic displacement values observed in that site

the integral of velocity, which is the static displacement:

$$\lim_{\omega\to 0}\tilde{\dot{u}}(\omega)=\int_{-\infty}^{\infty}\dot{u}(t)\mathrm{d}t=u(\infty). \tag{1}$$

Although this property is verified in the PSGCX records it may be difficult to use in practice because of noise and limited frequency band. Anyway, the high quality of northern Chile accelerographs and the high signal/noise ratio allow us to obtain in some cases the static displacement directly from velocity spectra using Eq. (1); see Fig. 6.

4. Why Omega-1?

Radiation from seismic sources can be approximated by the radiation from a point double couple inside a homogeneous medium (see Aki and Richards 2002 and the Appendix). Modifying slightly the first term in Equation (7), the radiation from a point seismic moment source is

$$\begin{aligned}u_i(r,t)=&\frac{1}{4\pi\rho\beta^2}A^N\frac{1}{r^2}\int_{\frac{\beta}{\alpha}}^{1}\tau M_0\left(\frac{\beta t}{r}-\tau\right)\mathrm{d}\tau\\&+\frac{1}{4\pi\rho\alpha^2}A^{\mathrm{IP}}\frac{1}{r^2}M_0\left(t-\frac{r}{\alpha}\right)+\frac{1}{4\pi\rho\beta^2}A^{\mathrm{IS}}\frac{1}{r^2}M_0\left(t-\frac{r}{\beta}\right)\\&+\frac{1}{4\pi\rho\alpha^3}A^{\mathrm{FP}}\frac{1}{r}\dot{M}_0\left(t-\frac{r}{\alpha}\right)+\frac{1}{4\pi\rho\beta^2}A^{\mathrm{FS}}\frac{1}{r}\dot{M}_0\left(t-\frac{r}{\beta}\right),\end{aligned} \tag{2}$$

where r is distance between the source and observer, and t is the time. The terms in the equation are usually called near, intermediate and far field. The A^i terms are the radiation patterns defined by Aki and Richards (2002). ρ,α,β are the density, P-wave and S-wave speeds, respectively. $M_0(t)$ is the seismic moment time history. The dot above the moment denotes moment rate. We wrote the first term of Eq. (2) in a slightly different form from Aki and Richards (2002) because we want to stress that the near and intermediate terms both decay as r^{-2} and cannot be separated in the study of radiation.

For the study of the spectrum of radiated waves, we rewrite the Fourier transform of (2) in the self-similar form:

$$\begin{aligned}\tilde{u}_i(r,\omega)=&\frac{M_0(\omega)}{r^2}\left[\frac{1}{4\pi\rho\alpha^2}F^{\mathrm{INP}}(\omega r/\alpha)e^{-\frac{i\omega r}{\alpha}}\right.\\&\left.+\frac{1}{4\pi\rho\beta^2}F^{\mathrm{INS}}(\omega r/\beta)e^{-\frac{i\omega r}{\beta}}\right]\\&+\frac{\dot{M}_0(\omega)}{r}\frac{1}{4\pi\rho\alpha^3}A^{\mathrm{FP}}e^{-\frac{i\omega r}{\alpha}}+\frac{1}{4\pi\rho\beta^3}A^{\mathrm{FS}}e^{-\frac{i\omega r}{\beta}},\end{aligned} \tag{3}$$

where $F^{\mathrm{INP}}(\omega r/\alpha)$ and $F^{\mathrm{INS}}(\omega r/\beta)$ are self-similar functions of frequency scaled by propagation time. They are defined in the appendix.

Expression (3) for the Green function in the frequency domain clearly shows that the near and intermediate field that decay as r^{-2} are proportional to moment, while the far field that decays like r^{-1} is proportional to moment rate. Since moment rate is known to be flat at low frequencies (i.e., proportional to ω^0), the near field is then inversely proportional to frequency, i.e., it behaves at low frequencies like ω^{-1}. We can show this property very simply by adopting Brune's (1970) source time function. Brune's moment rate is

$$\dot{M}(t)=M_0\omega_0^2te^{-\omega_0 t}H(t), \tag{4}$$

whose Fourier transform is:

$$\dot{M}_0(\omega)=M_0\frac{1}{\left(1+\frac{i\omega}{\omega_0}\right)^2}. \tag{5}$$

Here, ω_0 is the corner frequency. The Fourier transform of $M_0(\omega)$ is that of (5) divided by $i\omega$.

4.1. A Simplified Model for S Waves

We can illustrate the properties of strong motion in the near field with a simplified model of S waves that we derived from an equivalent model for P waves proposed by Vidale et al. (1995). From the previous theoretical considerations, we write a very simplified version of (2) that retains its main features. We consider only S waves that have Brune's (1970) waveform (4) in the time domain:

$$u(r,t)=\frac{C^{\mathrm{NF}}}{r^2}M_0\left(t-\frac{r}{\beta}\right)+\frac{C^{\mathrm{FF}}}{r}\dot{M}_0\left(t-\frac{r}{\beta}\right). \tag{6}$$

C^{NF} contains the near-field radiation pattern and normalization. C^{FF} contains the far-field radiation pattern and normalization. Expression (6) is a simple

way of writing the main features of the radiated waves from a point dislocation including a Brune finite source time function. Of course any other source time function can be used in this approximation.

In Fig. 7, we show a wave form in the near field computed using (6) that simulates quite well those observed in the EW component for large subduction earthquakes in Chile. We assumed a corner frequency $\omega_0 = 4 (f_0 = 0.637\text{Hz})$ and a ratio $C = \frac{C_{\text{NF}}}{rC_{\text{FF}}} = 0.75$ between the near- and far-field coefficients in (6). In the same figure, we show the spectrum computed using the exact transforms of the moment and moment rate. We observe that for these particular parameters, the peak displacement—dominated by the moment rate—is about twice the static displacement—dominated by the moment—in the time domain. Any other ratio of peak to static amplitude can be obtained by changing the ratio of the coefficients or the corner frequency. On the other hand, for this particular set of parameters (ω_0, C), the static field dominates the spectrum in most of the frequency range displayed in the figure. Moment rate becomes dominant only at frequencies larger than 2 Hz, well beyond the corner frequency. The interplay between the near-field and far-field terms is complex and depends on several parameters: the radiation pattern and distance that determine the coefficient C; and the corner frequency ω_0, that is inversely proportional to the duration. Thus, as we will elaborate in the discussion, the relative weight of near- and far-field terms depends on the relative values of the duration and the P–S time.

5. *Ground Motion Spectrum in Northern Chile After the Iquique Earthquake*

In the previous section, we studied the spectrum at station PSGCX (Pisagua) in northern Chile. This is

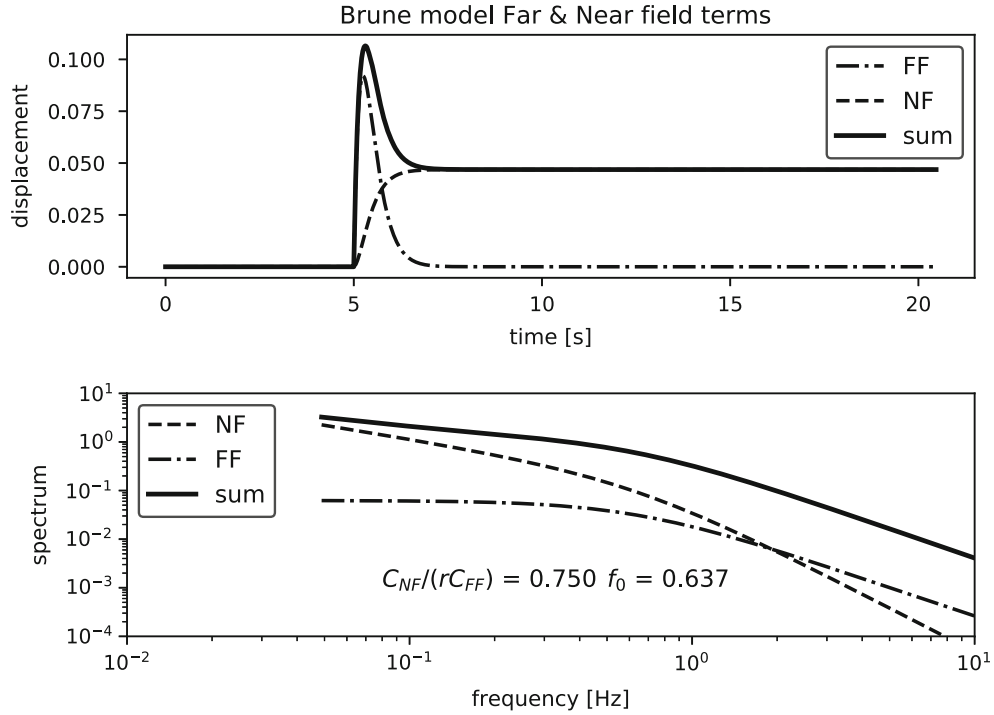

Figure 7

Spectra of a simplified near-field displacement spectrum computed for an S wave that contains both near- and far-field components. The near field is plotted with a dashed line and the far-field (Brune) signal is plotted with a dash-dotted line. The thick black line is the full near-field displacement signal. In this case, the ratio between the peak displacement and the static displacement is 2. The displacement spectrum is shown at the bottom with the same convention for the far- and near-field components. We observe that the near field (in black) dominates the spectrum for a very broad range of frequencies up to the corner frequency, which here is 0.637 Hz ($\omega_0 = 4\text{rad/s}$). The ratio between the coefficients in Eq. (6) is 0.75

the closest station to the earthquake epicenter and, as shown in the previous section, its displacement spectrum is dominated by the ω^{-1} low-frequency decay (Fig. 4) due to the finite jump in displacement observed in Fig. 3. At this distance, the seismic moment-dependent terms in the Green function, first term in (3), dominate the spectrum. As shown in Fig. 1 and Table 1, the Iquique earthquake was recorded at more than 20 accelerometric stations in northern Chile.

Let us first consider the PB11 station, which, as observed from Fig. 1, is situated some 60 km inland from Pisagua and located 119 km from the immediate foreshock of the earthquake. Figure 8 shows the EW component of displacement at this station. Displacement was computed by the Boore (2001) procedure discussed earlier. Superimposed on the seismic displacement trace, we plot the ground displacement determined at the same station from the GNSS antenna of the PB11 IPOC multi-parametric station. The traces for both the integrated accelerogram and the geodetic data are very similar and have a large static component. It is obvious that in this station the field is dominated by the moment time function. In the two bottom panels of Fig. 8, we show the ground displacement spectrum determined from the accelerogram spectrum by double Fourier integration (division by omega-2) and the velocity spectrum. The displacement spectrum shows the characteristic omega-1 behavior at low frequency, as expected from the static displacement observed in the displacement. The velocity spectrum at the bottom has the typical flat spectrum observed in northern Chile for the Iquique earthquake. The level of the flat part of the velocity spectrum is very close to the static displacement observed in the GNSS instrument trace (GPS) at the top of Fig. 8. This confirms relation (1) derived earlier.

As we move away from the source, the level of ground displacement decreases, yet the spectra are still dominated by the static displacement, and thus by the moment time function, rather than moment rate. We illustrate this with the record obtained at station PB01 of the IPOC network (see Fig. 1). This station is located near 21°S, about 219 km from the initial foreshock of the Iquique earthquake. Figure 9 shows the displacement records obtained from the accelerogram and the GNSS instruments of the PB01 IPOC station. Both coincide very well in the large amplitude part in the 60–100 s window and they diverge near the end of the record where the displacement is less than 2.5 cm. The spectra shown in the two bottom panels are very similar to those of the PB11 station. The flat part of the ground velocity spectrum is about 0.05 m, as shown with horizontal line in Fig. 9. Clearly, the velocity spectrum integrated from the accelerograms is determined by the static displacement produced by the earthquake at this station.

The similarity of the ground velocity spectra recorded at different distances from the Iquique earthquake is striking. In Fig. 10, we show a stack of the ground velocity spectra computed for several stations in northern Chile that recorded the Iquique earthquake.

The stations chosen for the plot of velocity spectra in Fig. 10 range in distance from 70 to 250 km, yet the spectra are very similar in the intermediate frequency range from 0.1 to 1 Hz. At lower frequencies, the spectra are dominated by the static field and thus by the moment time function. These spectra scale with the static displacement as shown in Figs. 9 and 10 for stations PB01 and PB11. In the high-frequency range, from 1 to 10 Hz, on the other hand, these spectra decay as omega-1 as predicted by Brune's model indicating that the high-frequency part is dominated by the moment rate–time function. In most of northern Chile, the spectra from the Iquique earthquake resemble those shown in the previous pictures, with strong contribution from the static near field. It is surprising that even at 219 km distance from the epicenter, at station PB01, shown in Fig. 9, the velocity spectra are still flat at the lowest resolvable frequencies.

Why do we observe the near field at such long distances? This is because the permanent co-seismic displacement induced by the moment tensor is still large at distances of the order of six times the size of the event. Although the near field decreases as r^{-2}, the ratio between far- and near-field terms decrease only as r^{-1} as shown in previous sections. Thus, the effect of the moment time function is still important at those distances.

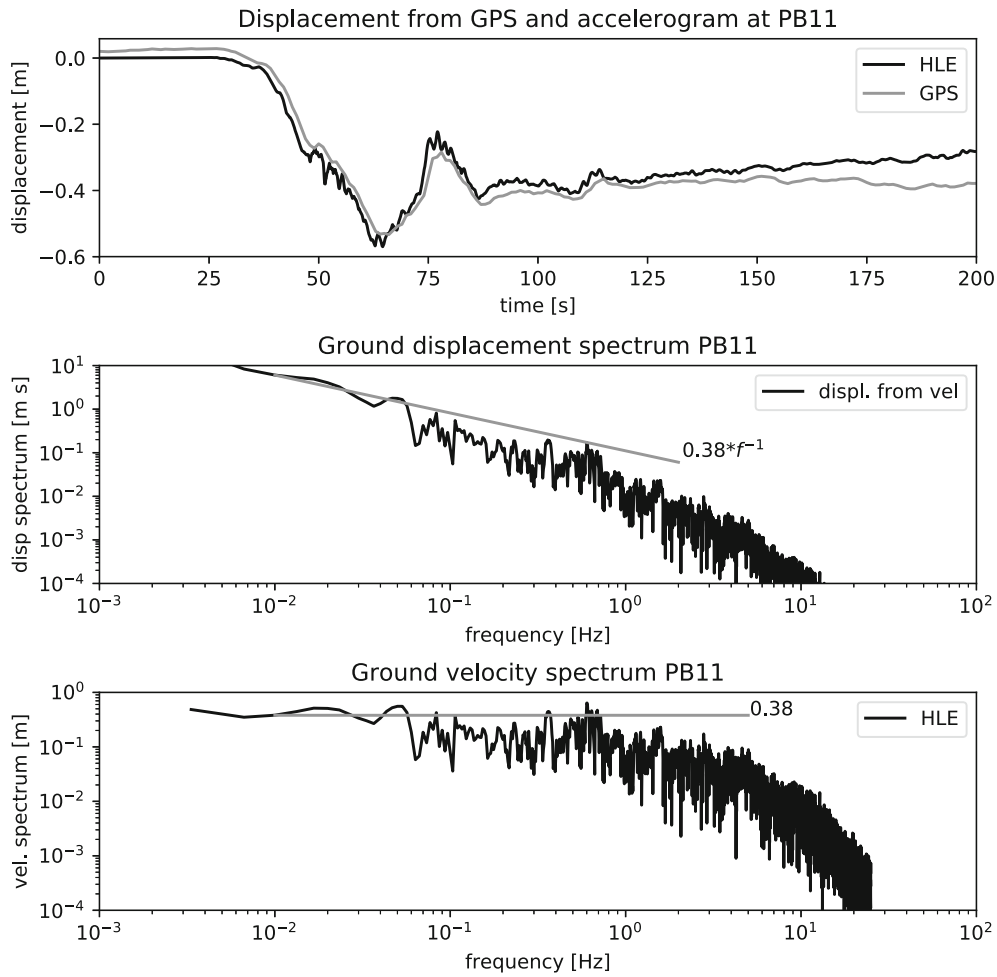

Figure 8
EW component of displacement integrated from the accelerogram of the PB11 station located 119 km from the epicenter of the 1 April 2014 Iquique earthquake of M_w 8.1. At the top, the displacement waveform computed by integrating the accelerogram is compared with the computed displacement from the co-located GNSS station. At the bottom, the displacement and velocity spectra computed from the accelerogram. The flat portion of the velocity spectrum fits very well the displacement jump of 0.38 m observed in the GNSS record. The ω^{-1} trend in the displacement spectrum fits nicely the trend derived from the velocity spectrum

6. *Transition to Aki–Brune Spectrum at Far Distances from the Source*

The previous section shows that in a very broad region around Iquique, the ground velocity spectra of the 1 April 2014 earthquake have similar low-frequency spectra dominated by the moment time function. We expected that as we move away from the source we should observe the emergence of a Brune like spectrum peaked at the corner frequency, i.e., proportional to ω at low frequencies and decreasing as ω^{-1} at higher frequencies. This is not obvious in the velocity spectra of Fig. 10 except that of station PB07, 257 km from the epicenter, which decreases at high frequencies as predicted by Aki (1967) and Brune (1970), but still has a strong low-frequency component.

To observe Brune's spectrum more clearly, we take a smaller event. We chose the foreshock of Iquique earthquake that occurred on 16 March 2014 near the south-west edge of the main rupture zone of the Iquique earthquake (see Fig. 1 for location). This is an M_w 6.7 event that had a somewhat different source mechanism than the main event (Ruiz et al.

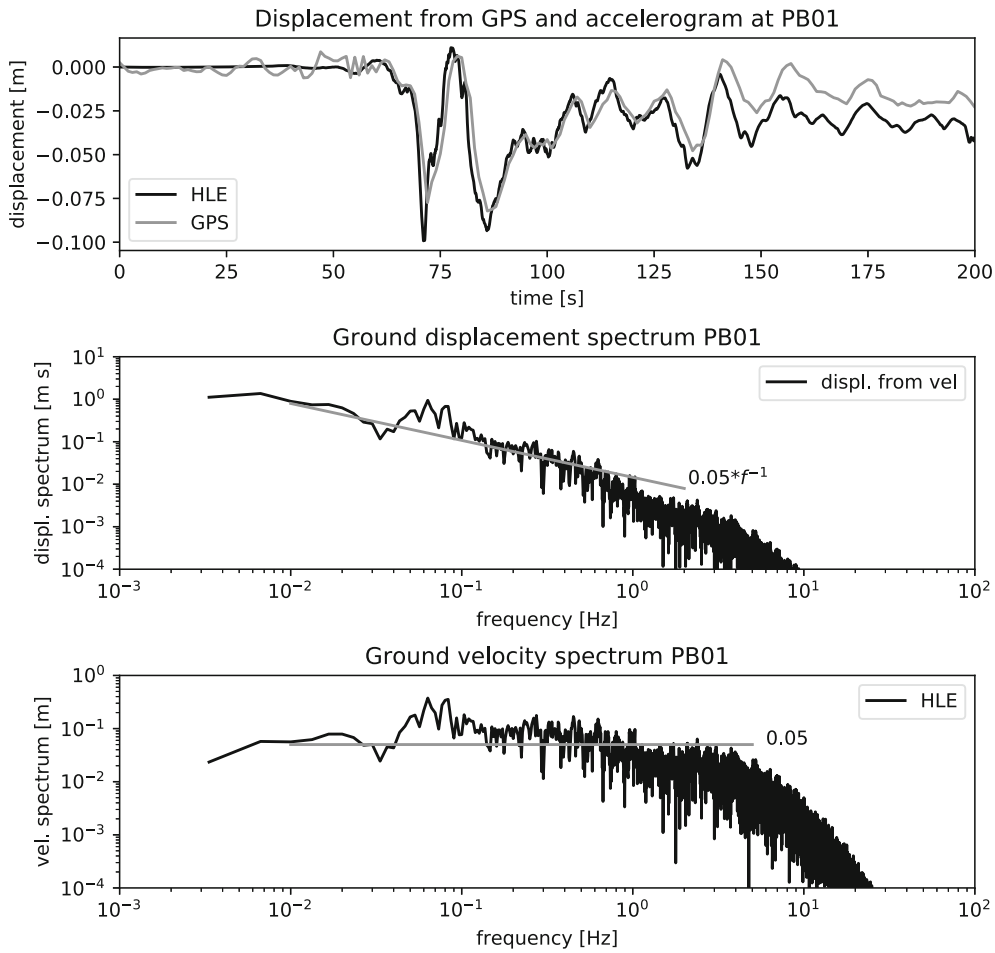

Figure 9
EW component of displacement integrated from the accelerogram of PB01 station located 219 km from the epicenter of the 1 April 2014 Iquique earthquake, M_w 8.1. At the top, the displacement integrated from the accelerograms is compared with the computed displacement from the collocated GNSS station. At the bottom, the displacement and velocity spectra computed from the accelerogram. The flat portion of the velocity spectrum fits very well the velocity jump observed in displacement. The ω^{-1} trend in the displacement spectrum fits nicely the trend derived from the velocity spectrum

2014; Leon-Ríos et al. 2016; Cesca et al. 2016). In Fig. 11, we plot two accelerograms generated by this earthquake. Stations PB11 and PB01 provide excellent recordings. The first is at 121 km, and the other at 150 km distance from an event that probably had a source size of about 10 km. For station PB11, it is still difficult to clearly separate the P- and S-wave trains in the integrated displacement trains. On the PB01 records, the P and S waves are very well separated so that we could identify an S window. This is indicated in red in the PB01 accelerogram and was isolated using multitaper spectral techniques (Park et al. 1987; Prieto et al. 2009). At central northern Chile stations, this event has the typical ω^{-2} high-frequency decay.

In Fig. 12, we plot the displacement spectra for the two stations of Fig. 11. At the PB01 station, we computed spectra both for the entire record and for the S-wave window shown here in red. The two spectra resemble many other spectra published in the literature for the largest local event recordings. The high-frequency decay is ω^{-2} beyond 1 Hz. They also have a flat spectrum plateau at low frequencies, for frequencies less than 0.1 Hz for the PB01

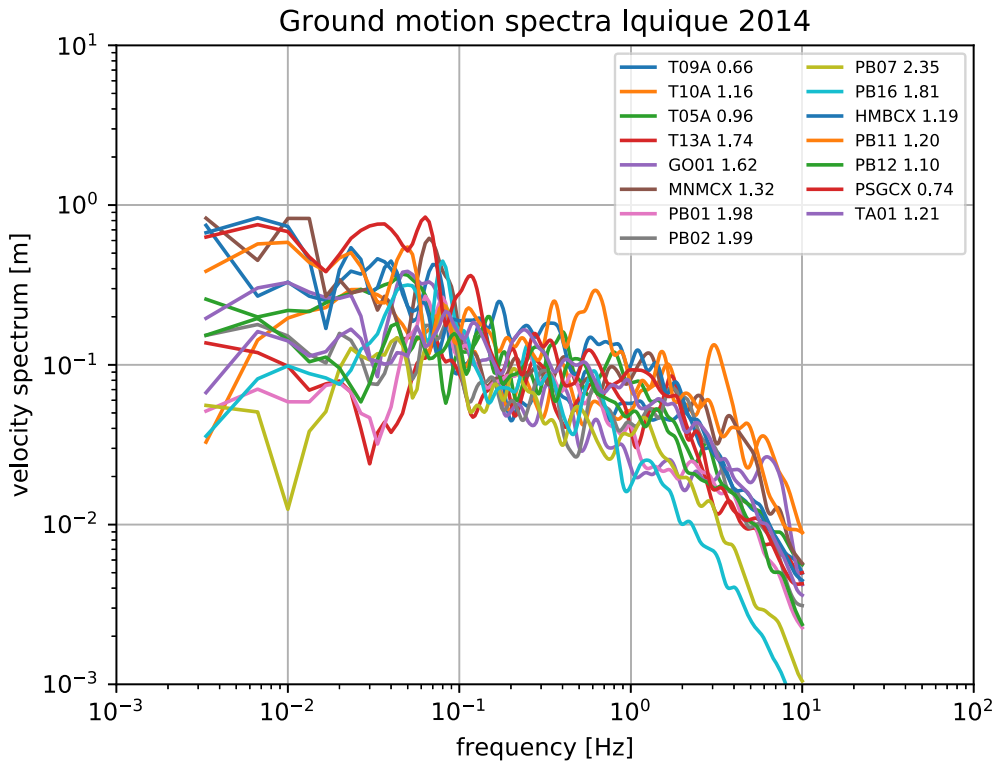

Figure 10
Stack of the EW component of velocity spectra observed at a set of selected strong motion stations in northern Chile. The spectra were smoothed using a Konno–Ohmachi filter. All other records resemble this group of spectra. The numbers next to the station codes are the epicentral distances of each station in degrees

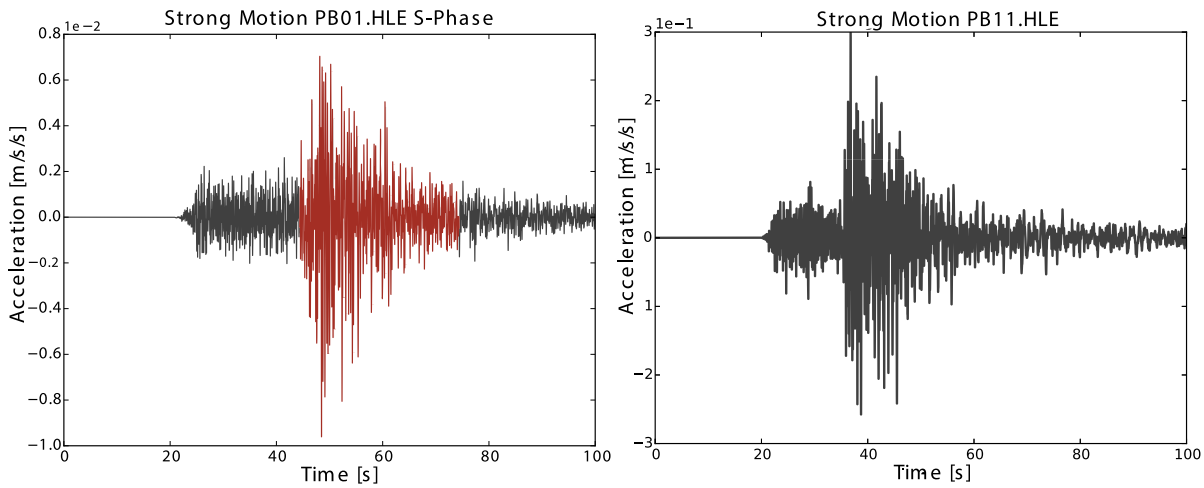

Figure 11
Accelerograms recorded at two IPOC stations PB01 and PB11 for the 16 March 2014 precursor of the Iquique earthquake of 1 April 2014. PB11 is at 121 km and PB01 at 256 km from the source. This event of M_w 6.7 is much smaller than the main shock

accelerogram. In Fig. 12 we show the spectrum computed for the whole record in black and the spectrum computed for the S-wave window in red. As expected, since S waves are much stronger than P waves, the whole record spectrum and the S-wave window spectrum are very similar.

The most important feature of these records is the presence of a broad spectral range where the spectra behave like ω^{-1}, as indicated by the thin grid superimposed on the spectra. The spectra do not exactly decay as ω^{-1}, but just have a broad transition region from 0.1 to 10 Hz. Intermediate frequency range with ω^{-1} decay have been reported by many authors [e.g., Denolle and Shearer (2016), Archuleta and Ji (2016), among others]. Archuleta and Ji (2016) observed those intermediate frequency ranges in the far field, while for the Iquique foreshock we cannot assume that the near field can be neglected. They explained the presence of the omega-1 trend with a modification of Brune's source time function (4). To properly model wave propagation in northern Chile and determine the relative contributions of the moment rate and moment time functions, we have to do a more detailed modeling of wave propagation. We are in the process of studying acceleration, GNSS and broadband records for the Valparaiso earthquake of 24 April 2017 that had excellent coverage in Central Chile (Ruiz et al. 2017a, 2018).

7. Discussion

It is surprising that the effect of the near field on the seismic spectra computed from the accelerograms of the 2014 Iquique earthquake has not been reported earlier. Many authors used these records for modeling the main event filtering out the low frequencies. One reason may be that the problems of integration of accelerograms (Boore 2001) discouraged the study of the spectral properties of seismic sources in the near field. An additional possible problem is that many standard routines used for processing accelerograms remove the trend assuming that the average velocity field is zero. In the near field, the average velocity is non-zero as proven by expression (1).

Our main observation is that the spectra of ground motion in the vicinity of an earthquake source contain two types of contributions: (1) the near-field terms that decay as r^{-2} with distance and are proportional to the seismic moment time function; (2) the other contribution is the far field that is proportional to moment rate and decays like r^{-1}.

While the P and S waves can be studied separately in the far field, in the near field they cannot be separated because they interfere to produce the static field. The terms that contribute to P or S waves decay individually like r^{-4} (Aki and Richards 2002), but interfere at low frequencies to produce a single r^{-2}

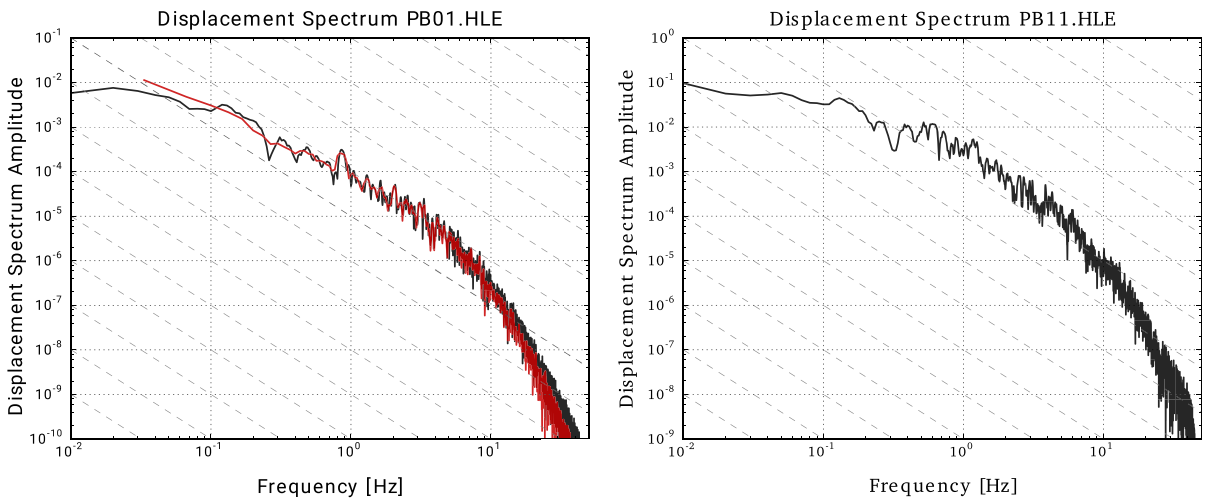

Figure 12
Displacement spectra of the two records shown in Fig. 11. Black spectra consider all records and red spectra the S-wave window

near-field contribution to strong motion (Eq. 3). This is the term that dominates the spectrum of all the accelerograms recorded after the 2014 Iquique earthquake in a range of less than 200 km from the epicenter of the earthquake. Further study of the properties of the near field requires more accurate numerical simulations including the free-surface effects and structural properties of wave propagation. The simple point source model used here provides a clear proof that near- and far-field terms in the accelerograms are equally important, but the effects of wave propagation must be taken carefully into account. Observations of the relative weight of near and far field have been reported earlier (Vidale et al. 1995; Jiao et al. 1995), but a systematic study of the spectral properties has not been done to our knowledge.

At what distance does the far-field spectrum become dominant? For the M_w 8.4, 2014 Iquique earthquake studied here, the near field dominates all the records out to 219 km. Only for smaller events studied in Sect. 5, a far-field spectrum resembling the Brune-Aki model appears at distant stations. Thus, the relative value of the near- and far-field terms depends not just on distance, but also on the duration of the source. Although we cannot provide a simple rule for the transition distance, we believe that the transition occurs beyond the distance at which the seismic source duration of the event is of the same order as the separation between P and S waves, for the Iquique earthquake with duration of 50 s, this distance is close to 400 km assuming an average P-wave speed of 6 km/s and an P/S velocity ratio of 1.73. A more detailed study including careful modeling of the interaction of surface reflections and guided waves is necessary to provide an accurate answer. A more accurate estimate will be the object of future work.

We proved from observations that, as expected from the properties of Fourier transform, the low-frequency velocity spectral amplitude converges to the co-seismic displacement observed in collocated GNSS instruments. Thus, it may be possible, in principle, to use velocity spectra to determine the static displacements as complement to GNSS data. Unfortunately, this requires acceleration traces with a good signal/noise ratio, located in hard rock sites to avoid non-linear site effects.

The stack of the displacement spectra observed in northern Chile after the Iquique earthquake (Fig. 10) shows that the velocity spectra in the frequency range between 0.1 and 1 Hz are very similar in all the stations. In the low-frequency range less than 0.1 Hz the spectra have variable amplitudes that scale with the static displacement at the site. This confirms the theoretical prediction that the level of the flat part of the velocity spectrum is proportional to the static ground displacement. These static levels can be computed by the usual techniques to predict static ground motion using Okada's (1985) formulas. As shown in Figs. 8 and 9 for stations PB01 and PB11, the low-frequency level of the velocity spectrum fits quite well with the static displacement observed by collocated GNSS instruments.

One of the main consequences of this study is that the classical scaling of the earthquake spectra (Aki 1967) does not hold for large earthquakes, for which the displacement spectra decay as omega-1 at low frequencies. This was first observed by Lancieri et al. (2012) in their study of the Tocopilla earthquake of 2007 and its aftershocks. Although few stations were available at the time, the aftershocks less than M_w 6 had spectra that matched the scaling law of Aki (1967) and Prieto et al. (2004).

The results reported here for the Iquique earthquake hold for most large events in Chile for which we have very good broadband accelerograms and GNSS recordings. We have observed omega-1 low-frequency displacement spectra for the 2010 Maule earthquake in two good-quality accelerograms and for other large events including the 2007, M_w 7.8 Tocopilla earthquake; the 2015, M_w 8.3 Illapel earthquake and the 2016 Chiloe earthquake of M_w 7.6. For events less than 7.0, we have explored just a few events, typically aftershocks of the larger events. The best data is for the Valparaíso earthquake of M_w 6.9 that occurred on 23 April 2017 (Ruiz et al. 2017a, 2018). The ground velocity spectrum for this event resembles that of a scaled down version of the Iquique earthquake studied here at close distances and then becomes similar to that of Brune's spectrum at longer distances from the source. The origin of the intermediate ω^{-1} slope in displacement spectra needs

further study and comparison with other events as reported by Archuleta and Ji (2016) and Denolle and Shearer (2016), among others, for far-field observations.

What are the consequences for ground motion prediction? A usual assumption about the spectrum of large earthquakes is that they have an omega-2 displacement spectrum and the spectra for large earthquakes is generated by summing—often random—combinations of small events. This assumption must be revised for large-magnitude synthetic strong motion simulations by adding a near-fault term. This problem was analyzed, among others, by Tumarkin et al. (1994) who showed that it was very difficult to produce an omega-2 spectrum by adding smaller point-like sources.

8. Conclusions

We have shown that the spectrum of ground motion in the vicinity of very large subduction earthquakes in northern Chile is quite different from that proposed by Aki and Brune, the so-called omega-2 spectrum, which is flat at low frequencies and decays as omega-2 at high frequencies. The spectrum in the near field is dominated by the seismic moment time function that contains static terms. This produces an omega-1 displacement spectrum at low frequencies. This kind of spectrum dominates radiation surprisingly far from the source, up to 250 km in the present case. We also find that separation of P and S waves is not possible because the P- and S-like near-field terms interfere to produce the static field of the earthquake.

9. Data

The data used for this study were downloaded mainly from Centro Sismologico Nacional of the University of Chile (CSN). For large Chilean earthquakes, the significant earthquake database of the CSN provides corrected records at the website (http://edb.csn_uchile.cl). Geodetic data are available also from the CSN at the GPS site (http://gps.csn.uchile.cl/). Additional information and data for the IPOC stations of northern Chile are available from the Geofon pages of the GFZ data center (https://geofon.gfz-potsdam.de/) and from the Wilber3 pages of the IRIS data center (http://ds.iris.edu/wilber3/).

Acknowledgements

This study was supported by FONDECYT contract No. 1170430 and by PRS (Programa Riesgo Sísmico of Universidad de Chile).

Appendix

From Aki and Richards (2002), the Green function for a point moment tensor source in a homogeneous elastic space is:

$$u_i(r,t) = \frac{1}{4\pi\rho}\frac{1}{r^4}A^N \int_{\frac{r}{\alpha}}^{\frac{r}{\beta}} \tau M_0(t-\tau)\mathrm{d}\tau + \frac{1}{4\pi\rho\alpha^2}A^{\mathrm{IP}}\frac{1}{r^2}M_0\left(t-\frac{r}{\alpha}\right) + \frac{1}{4\pi\rho\beta^2}A^{\mathrm{IS}}\frac{1}{r^2}M_0\left(t-\frac{r}{\beta}\right) + \frac{1}{4\pi\rho\alpha^3}A^{\mathrm{FP}}\frac{1}{r}\dot{M}_0\left(t-\frac{r}{\alpha}\right) + \frac{1}{4\pi\rho\beta^3}A^{\mathrm{FS}}\frac{1}{r}\dot{M}_0\left(t-\frac{r}{\beta}\right). \quad (7)$$

It is usually assumed that the near-field term (the first one) decays as r^{-4}, but this is actually not correct because the time integral on the left grows like r^2 with distance r from the source. It is possible to rewrite the integral changing variables to $\tau = \vartheta\frac{r}{\beta}$, where ϑ is non-dimensional. Equation (7) becomes (3) of the main text that clearly shows that the first term behaves as r^{-2}, like those of the intermediate field.

We can now determine the spectrum of (7) using the continuous Fourier transform:

$$\tilde{u}(\omega) = \int_{-\infty}^{\infty} u(t)e^{-i\omega t}\mathrm{d}t. \quad (8)$$

We observe that the integral of the first line in (7) is a convolution, so that its Fourier transform is

$$\tilde{M}_0(\omega)\int_{\frac{r}{\alpha}}^{\frac{r}{\beta}}\tau e^{-i\omega\tau}\mathrm{d}\tau=\tilde{M}_0(\omega)\frac{1}{\omega^2}\left[\left(\frac{i\omega r}{\alpha}+1\right)e^{-i\omega r/\alpha}-\left(\frac{i\omega r}{\beta}+1\right)e^{-i\omega r/\beta}\right]. \quad (9)$$

That can be compared to similar expressions from Aki and Richards (2002), taking into account that they used a different definition of the Fourier transform (8) than us. Taking the Fourier transform of (7), using (9) and collecting the terms that depend on $\tilde{M}_0(\omega)$ we get:

$$\begin{aligned}\tilde{u}_i(r,\omega)=&\frac{1}{4\pi\rho\beta^2}\frac{1}{r^2}\tilde{M}_0(\omega)\frac{A^N\beta^2}{\omega^2r^2}\left[\left(\frac{i\omega r}{\alpha}+1\right)e^{-i\omega r/\alpha}-\left(\frac{i\omega r}{\beta}+1\right)e^{-i\omega r/\beta}\right]\\&+\frac{1}{4\pi\rho\alpha^2}\frac{1}{r^2}\tilde{M}_0(\omega)A^{\mathrm{IP}}e^{-\frac{i\omega r}{\alpha}}+\frac{1}{4\pi\rho\beta^2}\frac{1}{r^2}\tilde{M}_0(\omega)A^{\mathrm{IS}}e^{-\frac{i\omega r}{\beta}}\\&+\frac{1}{4\pi\rho\alpha^3}\frac{1}{r}\dot{\tilde{M}}_0(\omega)A^{\mathrm{FP}}e^{-\frac{i\omega r}{\alpha}}+\frac{1}{4\pi\rho\beta^3}\frac{1}{r}\dot{\tilde{M}}_0(\omega)A^{\mathrm{FS}}e^{-\frac{i\omega r}{\beta}}.\end{aligned} \quad (10)$$

Expression (10) shows that there are two types of terms, those that depend on moment which are also inversely proportional to r^2 and those that depend on moment rate and are inversely proportional to radius r. Gathering all the moment-dependent terms we get the expression of Eq. (4) in the text. The non-dimensional coefficients F^{INP} and F^{INS} are given by:

$$F^{\mathrm{NIP}}\left(\frac{\omega r}{\alpha}\right)=A^N\frac{\alpha^2}{\omega^2r^2}\left(\frac{i\omega r}{\alpha}+1\right)+A^{\mathrm{IP}},$$

$$F^{\mathrm{NIS}}\left(\frac{\omega r}{\beta}\right)=-A^N\frac{\beta^2}{\omega^2r^2}\left(\frac{i\omega r}{\beta}+1\right)+A^{\mathrm{IS}}.$$

These are non-dimensional functions that depend only on non-dimensional frequency $\omega r/a$ *or* $\omega r/\beta$ and the radiation patterns.

References

Abercrombie, R. E. (1995). Earthquake source scaling relationships from − 1 to 5 ML using seismograms recorded at 2.5-km depth. *Journal of Geophysical Research, 100,* 24015–24036.

Aki, K. (1967). Scaling law of seismic spectrum. *Journal of Geophysical Research, 73,* 5359–5376.

Aki, K., & Richards, P. G. (2002). *Quantitative seismology*. USA: University Science Books. ISBN 978-1-891389-63-4.

Allmann, B. P., & Shearer, P. M. (2009). Global variations of stress drop for moderate to large earthquakes. *Journal of Geophysical Research, 114,* B01310. https://doi.org/10.1029/2008jb005821.

Archuleta, R. J., & Ji, C. (2016). Moment rate scaling for earthquakes 3.3 ≤ *M* ≤ 5.3 with implications for stress drop. *Geophysical Research Letters*, *43*(23), 12004–12011.

Báez, J. C., Leyton, F., Troncoso, C., del Campo, F., Bevis, M., Vigny, C., et al. (2018). The Chilean GNSS network: Current status and progress toward early warning applications. *Seismological Research Letters*, *89*, 1546–1554.

Barrientos, S., & National Seismological Center (CSN). (2018). The seismic network of Chile. *Seismological Research Letters, 89,* 467–474.

Bock, Y., Melgar, D., & Crowell, B. W. (2011). Real-time strong-motion broadband displacements from collocated GPS and accelerometers. *Bulletin of the Seismological Society of America, 101,* 2904–2925.

Boore, D. M. (2001). Effect of baseline corrections on displacements and response spectra for several recordings of the 1999 Chi-Chi, Taiwan, earthquake. *Bulletin of the Seismological Society of America, 91,* 1199–1211.

Boore, D. M., & Bommer, J. J. (2005). Processing of strong-motion accelerograms: Needs, options and consequences. *Soil Dynamics and Earthquake Engineering, 25,* 93–115.

Brune, J. (1970). Tectonic stress and the spectra of seismic shear waves from earthquakes. *Journal of Geophysical Research, 75,* 4997–5009.

Cesca, S., Grigoli, F., Heimann, S., Dahm, T., Kriegerowski, M., Sobiesiak, M., et al. (2016). The M_w 8.1 2014 Iquique, Chile, seismic sequence: A tale of foreshocks and aftershocks. *Geophysical Journal International, 204,* 1766–1780.

Chao, W., Wu, Y., & Zhao, L. (2009). An automatic scheme for baseline correction of strong-motion records in coseismic deformation determination. *Journal of Seismology, 14,* 495–504.

Delouis, B., & Legrand, D. (2007). M_w 7.8 Tarapaca intermediate depth earthquake of 13 June 2005 (northern Chile): Fault plane identification and slip distribution by waveform inversion. *Geophysical Research Letters.* https://doi.org/10.1029/2006gl028193.

Delouis, B., Pardo, M., Legrand, D., & Monfret, T. (2009). The M_w 7.7 Tocopilla earthquake of 14 November 2007 at the southern edge of the northern Chile seismic gap: Rupture in the deep part of the coupled plate interface. *Bulletin of the Seismological Society of America, 99,* 87–94.

Denolle, M. A., & Shearer, P. M. (2016). New perspectives on self-similarity for shallow thrust earthquakes. *Journal of Geophysical Research, 121,* 6533–6565.

Duputel, Z., Jiang, J., Jolivet, R., Simons, M., Rivera, L., Ampuero, J. P., et al. (2015). The Iquique earthquake sequence of April 2014: Bayesian modeling accounting for prediction uncertainty. *Geophysical Research Letters, 42,* 7949–7957.

Fuenzalida, A., Schurr, B., Lancieri, M., & Madariaga, R. (2013). High resolution relocation and mechanism of aftershocks of the 2007 Sobiesiak M. and Tocopilla (Chile) earthquake. *Geophysical Journal International, 194,* 1216–1238.

Graizer, V. M. (1979). Determination of the true displacement of the ground from strong-motion recordings. *Izv. USSR Academy of Sciences, Physics Solid Earth, 15,* 875–885.

Graizer, V. (2010). Strong motion recordings and residual displacements: What are we actually recording in strong motion seismology? *Seismological Research Letters, 81,* 635–639.

Hayes, G. P., Herman, M. W., Barnhart, W. D., Furlong, K. P., Riquelme, S., Benz, H. M., et al. (2014). Continuing megathrust earthquake potential in Chile after the 2014 Iquique earthquake. *Nature, 512*(7514), 295–298.

Hoffmann, F., Metzger, S., Moreno, M., Deng, Z., Sippl, C., Ortega-Culaciati, F., & Oncken, O. (2018). Characterizing afterslip and ground displacement rate increase following the 2014 Iquique-Pisagua M_w 8.1 earthquake, Northern Chile. *Journal of Geophysical Research*, *123*, 4171–4192. https://doi.org/10.1002/2017JB014970.

Ide, S., & Beroza, G. C. (2001). Does apparent stress vary with earthquake size? *Geophysical Research Letters, 28,* 3349–3352.

IPOC. (2006). GFZ German Research Centre for Geosciences; Institut des Sciences de l'Univers-Centre National de la Recherche CNRS-INSU: IPOC Seismic Network. Integrated Plate boundary Observatory Chile—IPOC. Other/Seismic Network. https://doi.org/10.14470/pk615318.

Iwan, W., Moser, M., & Peng, C. (1985). Some observations on strong motion earthquake measurement using a digital acceleration. *Bulletin of the Seismological Society of America, 75,* 1225–1246.

Jiao, W., Wallace, T. C., Beck, S., Silver, P. G., & Zandt, G. (1995). Evidence fir static displacements from the June 9, 1994 deep Bolvian earthquake. *Geophysical Research Letters, 22,* 2285–2288.

Kato, A., & Nakagawa, S. (2014). Multiple slow-slip events during a foreshock sequence of the 2014 Iquique, Chile M_w 8.1 earthquake. *Geophysical Research Letters, 41,* 5420–5427.

Lancieri, M., Madariaga, R., & Bonilla, F. (2012). Spectral scaling of the aftershocks of the Tocopilla 2007 earthquake in northern Chile. *Geophysical Journal International, 188,* 469–480.

Lange, D., Ruiz, J., Carrasco, S., & Manríquez, P. (2017). The Chiloé M_w 7.6 earthquake of 25 December 2016 in Southern Chile and its relation to the M_w 9.5 1960 Valdivia earthquake. *Geophysical Journal International, 213,* 210–277.

Lay, T., Yue, H., Brodsky, E. E., & An, C. (2014). The 1 April 2014 Iquique, Chile, M_w 8.1 earthquake rupture sequence. *Geophysical Research Letters, 41,* 3818–3825.

Leon-Ríos, S., Ruiz, S., Maksymowicz, A., Leyton, F., Fuenzalizada, A., & Madariaga, R. (2016). Diversity of the Iquique's foreshocks and aftershocks: A clue about complex rupture process of a M_w 8.1 earthquake. *Journal of Seismology, 20,* 1059–1073.

Leyton, F., Leopold, A., Hurtado, G., Pasten, C., Ruiz, S., Montalva, G., et al. (2018a). Geophysical characterization of the Chilean seismological stations: First results. *Seismological Research Letters*. https://doi.org/10.1785/0220170156.

Leyton, F., Pasten, C., Ruiz, S., Idini, B., & Rojas, F. (2018b). Empirical site classification of CSN network using strong-motion records. *Seismological Research Letters*. https://doi.org/10.1785/0220170167.

Madariaga, R. (1976). Dynamics of an expanding circular fault. *Bulletin of the Seismological Society of America, 65,* 163–182.

Madariaga, R., & Ruiz, S. (2016). Earthquake dynamics on circular faults: a review 1970–2015. *Journal of Seismology, 20,* 1059–1073.

Melgar, D., Fan, W., Riquelme, S., Geng, J., Liang, C., Fuentes, M., et al. (2016). Slip segmentation and slow rupture to the trench during the 2015, M_w 8. 3 Illapel, Chile earthquake. *Geophysical Research Letters, 43,* 961–966.

Melgar, D., Riquelme, S., Xu, X., Baez, J. C., Geng, J., & Moreno, M. (2017). The first since 1960: A large event in the Valdivia segment of the Chilean Subduction Zone, the 2016 *M*7.6 Melinka earthquake. *Earth and Planetary Science Letters, 474,* 68–75.

Okada, Y. (1985). Surface deformation due to shear and tensile faults in a half-space. *Bulletin of the Seismological Society of America, 75,* 1135–1154.

Oth, A., Bindi, D., Parolai, S., & Di Giacomo, D. (2010). Earthquake scaling characteristics and the scale-(in) dependence of seismic energy-to-moment ratio: Insights from KiK-net data in Japan. *Geophysical Research Letters, 37,* L19304. https://doi.org/10.1029/2010gl044572.

Park, J., Lindberg, C. R., & Vernon, F. L. (1987). Multitaper spectral analysis of high-frequency seismograms. *Journal of Geophysical Research*, *92*(B12), 12675–12674.

Peyrat, S., Campos, J., De Chabalier, J. B., Perez, A., Bonvalot, S., Bouin, M. P., et al. (2006). Tarapacá intermediate-depth earthquake (M_w 7.7, 2005, northern Chile): A slab-pull event with horizontal fault plane constrained from seismologic and geodetic observations. *Geophysical Research Letters*. https://doi.org/10.1029/2006gl027710.

Peyrat, S., Madariaga, R., Buforn, E., Campos, J., Asch, G., & Vilotte, J. P. (2010). Kinematic rupture process of the 2007 Tocopilla earthquake and its main aftershocks from teleseismic and strong-motion data. *Geophysical Journal International, 182,* 1411–1430.

Prieto, G. A., Parker, R. L., & Vernon, F. L, I. I. I. (2009). A Fortran 90 library for multitaper spectrum analysis. *Computers & Geosciences*, *35*(8), 1701–1710.

Prieto, G. A., Shearer, P. M., Vernon, F. L., & Kilb, D. (2004). Earthquake source scaling and self-similarity estimation from stacking P and S spectra. *Journal of Geophysical Research*. https://doi.org/10.1029/2004jb003084.

Ruiz, S., Aden-Antoniow, F., Baez, J. C., Otarola, C., Potin, B., del Campo, F., et al. (2017a). Nucleation phase and dynamic inversion of the M_w 69 Valparaíso 2017 earthquake in Central Chile. *Geophysical Research Letters*. https://doi.org/10.1002/2017gl075675.

Ruiz, J. A., Contreras-Reyes, E., Ortega-Culaciati, F., & Manríquez, P. (2018). Rupture process of the April 24, 2017, M_w 6.9 Valparaíso earthquake from the joint inversion of teleseismic body waves and near-field data. *Geophysical Research Letters, 279,* 1–14.

Ruiz, S., Klein, E., del Campo, F., Rivera, E., Poli, P., Metois, M., et al. (2016). The seismic sequence of the 16 September 2015, Illapel M_w 8.3 earthquake. *Seismological Research Letters, 87,* 789–799.

Ruiz, S., & Madariaga, R. (2018). Historical and recent large Megathrust earthquakes in Chile. *Tectonophysics, 733,* 37–56.

Ruiz, S., Madariaga, R., Astroza, M., Saragoni, G. R., Lancieri, M., Vigny, C., et al. (2012). Short period rupture process of the 2010 M_w 8.8 Maule earthquake in Chile. *Earthquake Spectra, 28*(S1), 1–18.

Ruiz, S., Metois, M., Fuenzalida, A., Ruiz, J., Leyton, F., Grandin, R., et al. (2014). Intense foreshocks and a slow slip event preceded the 2014 Iquique M_w 8.1 earthquake. *Science, 345,* 1165–1169.

Ruiz, S., Moreno, M., Melnick, D., Campo, F., Poli, P., Baez, J. C., et al. (2017b). Reawakening of large earthquakes in South-

Central Chile: The 2016 M_w 76 Chiloe event. *Geophysical Research Letters*. https://doi.org/10.1002/2017gl074133.

Schurr, B., Asch, G., Hainzl, S., Bedford, J., Hoechner, A., Palo, M., et al. (2014). Gradual unlocking of plate boundary controlled initiation of the 2014 Iquique earthquake. *Nature, 512,* 299–302.

Schurr, B., Asch, G., Rosenau, M., Wang, R., Oncken, O. & Barrientos, S. (2012). The 2007 M7. 7 Tocopilla northern Chile earthquake sequence: Implications for along-strike and downdip rupture segmentation and megathrust frictional behavior. Journal of Geophysical Research: Solid Earth, 117 (B5).

Socquet, A., Valdes, J. P., Jara, J., Cotton, F., Walpersdorf, A., Cotte, N., et al. (2017). An 8 month slow slip event triggers progressive nucleation of the 2014 Chile megathrust. *Geophysical Research Letters, 44,* 4046–4053.

Tilmann, F., Zhang, Y., Moreno, M., Saul, J., Eckelmann, F., Palo, M., et al. (2016). The 2015 Illapel earthquake, central Chile: A type case for a characteristic earthquake? *Geophysical Research Letters, 43,* 574–583.

Tumarkin, A. G., Archuleta, R., & Madariaga, R. (1994). Basic scaling rules for composite earthquake models. *Bulletin of the Seismological Society of America, 54,* 1279–1883.

Vidale, J., Goes, S., & Richards, P. G. (1995). Near-field deformation seen on distant broad band seismograms. *Geophysical Research Letters, 22,* 1–4.

Vigny, Ch., Socquet, A., Peyrat, S., Ruegg, J.-C., Metois, M., Madariaga, R., et al. (2011). The 2010 M_w 8.8 Maule mega-thrust earthquake of central Chile, monitored by GPS. *Science, 331,* 1417–1421.

Wang, G., Boore, D. M., Igel, H., & Zhou, X. (2003). Some observations on colocated and closely spaced strong ground-motion records of the 1999 Chi-Chi, Taiwan, earthquake. *Bulletin of the Seismological Society of America, 93,* 674–693.

Wang, R., Parolai, S., Ge, M., Jin, M., Walter, T. R., & Zschau, J. (2013). The 2011 M_w 9.0 Tohoku earthquake: Comparison of GPS and strong-motion data. *Bulletin of the Seismological Society of America, 103,* 1336–1347.

Wang, R., Schurr, B., Milkereit, C., Shao, Zh, & Jin, M. (2011). An improved automatic scheme for empirical baseline correction of digital strong-motion records. *Bulletin of the Seismological Society of America, 101,* 2029–2044.

Wu, Y., & Wu, C. (2007). Approximate recovery of coseismic deformation from Taiwan strong-motion records. *Journal of Seismology, 11,* 159–170.

Ye, L., Lay, T., Kanamori, H., & Koper, K. D. (2016). Rapidly estimated seismic source parameters for the 16 September 2015 Illapel, Chile M_w 8.3 earthquake. *Pure and Applied Geophysics, 173,* 321–332.

(Received June 1, 2018, revised August 17, 2018, accepted August 22, 2018)